TWO-DIMENSIONAL MODE-II DELAMINATION GROWTH IN COMPOSITE LAMINATES

Congzhe Wang, Anastasios P. Vassilopoulos and Thomas Keller

Composite Construction Laboratory (CCLab), Ecole Polytechnique Fédérale de Lausanne (EPFL), Station 16, Bâtiment BP, CH-1015 Lausanne, Switzerland

Keywords: 2D delamination, Mode II, Composite laminates, Fracture process zone

ABSTRACT

The available standards for fracture testing of fiber polymer composites are typically based on beam-like specimens, which may however not represent a real delamination growth phenomenon, where an embedded crack propagates in multiple directions with a changing contour. In this work, the two-dimensional (2D) delamination growth behavior was investigated using a novel experimental set-up. Circular plate specimens were semi-clamped along the edge allowing sliding movement and loaded transversally at the center above the embedded pre-crack. A rising load-deflection trend was observed even after rapid crack propagation due to the increasing crack-front length. Specimens with two different pre-crack sizes reached similar load, deflection and delamination area at failure. Under post-inspection using a digital microscope, a large-scale fracture process zone, including fiber bridging and hackles reflecting microcracking, was observed in the specimens.

1 INTRODUCTION

Fiber polymer composites are widely recognized for their superb mechanical performance in the direction of reinforcements, although exhibiting relatively low resistance against interlaminar shear and tension, making the separation of adjacent layers, i.e., delamination, the principal failure mode in such materials [1]. Considerable efforts have been devoted to the study of delamination, and several standards have been established, e.g., double cantilever beam (DCB) tests for Mode I, end-loaded spilt (ELS) tests and end-notched flexure (ENF) tests for Mode II, and mixed-mode bending (MMB) tests for mixed-Mode [2–5], all using one-dimensional (1D) beam-like specimens. Numerous works have been conducted based on such specimens, e.g., [6–8]. However, delamination in real structures will likely grow in multiple directions in the delamination plane, thus presenting a two-dimensional (2D) pattern. It becomes therefore questionable to use 1D tests to represent the delamination behavior of a more complicated structure.

Direct investigations of the growth of an embedded crack can be found in the studies on delamination buckling [9–12]. The crack front in such cases is usually under a Mode-I dominant condition with a changing mixed-mode ratio due to the complex stress states, making the 2D fracture analyses quite challenging. As a result, most delamination buckling and corresponding post-buckling analyses employed fracture properties extracted from 1D tests [11–13]. Another research area involving 2D fracture behavior of composites is the (low-velocity) impact delamination. Strategies for damage prediction in carbon fiber laminates subjected to low-velocity impact have been developed, relating the critical impact force to the Mode II critical strain energy release rate (SERR), G_{IIc} [14, 15]. Furthermore, impact experiments have been suggested as an alternative method for determining G_{IIc} and reasonable agreement has been observed between the results obtained from impact tests and standardized beam tests [16]. In fact, analyzing impact delamination within the context of fracture mechanics is challenging due to the involvement of multiple interface cracks with varying depths and the presence of other damage mechanisms, as well as the rate-dependent behavior of SERR and force signal oscillations [17]. Other types of 2D shear-mode delamination experiments have been conducted, such as three-point bending tests on wide beams with embedded elliptical pre-cracks [18] and investigations of edge delamination in circular plates under uniform water pressure [19]. Nevertheless, all the works mentioned above omitted the 2D effects on the delamination.

Kumar and Reddy [20] performed debonding experiments on circular bonded-plexiglass plates with a central circular pre-crack to simulate 2D fracture. The analytical estimation of the critical Mode-I SERR, G_{Ic}, neglecting geometric nonlinearity, yielded a value 33% lower than that obtained from double cantilever beam (DCB) specimens. However, recent works by Cameselle-Molares et al. [21–23] and the authors [24] reached a different conclusion for 2D delamination in composite laminates with significant fiber bridging. These studies employed a similar experimental setup to Ref. [20], using square plates opened transversely at the embedded circular pre-crack. Surprisingly, the load continued to rise after crack propagation, and the 2D G_{Ic} value determined through nonlinear numerical simulations was 40-50% higher than that from DCB experiments. The mentioned references focus on fracture conditions dominated by Mode-I behavior only, with no available literature specifically characterizing 2D Mode-II delamination.

This paper aims to experimentally investigate the growth of 2D Mode-II delamination in composite laminates and identify the 2D effects. A novel experimental setup was developed, involving circular laminated plates with different sizes of embedded circular pre-cracks. The plates were subjected to transverse loading at the center while being semi-clamped along the edge to promote circular-symmetric Mode-II delamination growth. Post-inspection using a digital microscope was conducted to examine the fracture process zone (FPZ), including large-scale fiber bridging and hackles reflecting micro-cracking.

2 EXPERIMENTAL PROGRAM

2.1 Material description

Fig. 1 presents the layup for the laminates employed, which consisted of two types of reinforcements: fourteen layers of E-CR glass (“Electrical” grade “Corrosion Resistant” glass) long continuous filament mats (CFM, Fig. 1b) without binder or stitching and six layers of E-glass multidirectional (quadriaxial 0/±45°/90°) sewed fabrics (MD, Fig. 1c). Epoxy resin (SikaBiresin CR83) was used as the matrix. The properties of the fibers and resin can be found in [21]. The layup employed exhibits the potential to promote large-scale fiber bridging between the inner CFM layers, which is likely to “augment” the 2D effects, while preventing premature flexural failure thanks to the stiffer outer MD layers. The adjacent MD layers were rotated by 22.5° to achieve in-plane quasi-isotropy. Good translucency was achieved allowing for direct crack observation, which was beneficial since non-destructive delamination detection usually requires sophisticated devices [25]. The asymmetric layup in the sub-laminates may introduce a slight mismatch between the curvature of the crack surfaces, but the resulting Mode-I component was deemed insignificant. In addition, tensile and double beam shear tests were conducted on six-layer CFM laminates and four-layer MD laminates to assess the corresponding material properties [26, 27] shown in Table 1. All laminates were manufactured using a vacuum infusion process, cured at room temperature for 16 hours under vacuum, and post-cured at 70°C for eight hours. The experiments included eight circular specimens with a radius of 180 mm, divided into two groups based on the pre-crack length (radius), a_0, as listed in Table 2. The pre-cracks were introduced using 13-μm-thick Teflon films during layup, and the specimens were waterjet cut, oven dried, and cooled before testing.

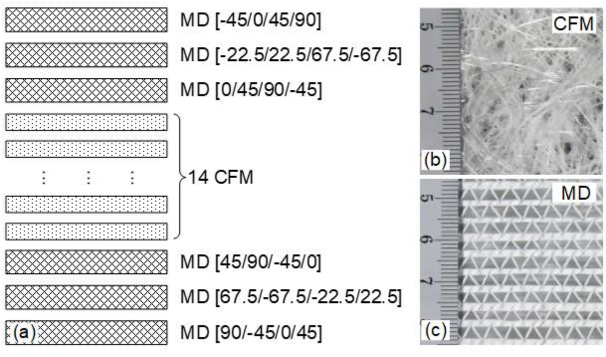

Fig. 1. Material description: (a) laminate layup, (b) CFM and (c) MD.

Reinforce-ment type	V_f (%)	E_1 (GPa)	E_2 (GPa)	E_3 (GPa)	ν_{12} (-)	ν_{13} (-)	ν_{23} (-)	G_{12} (GPa)	G_{13} (GPa)	G_{23} (GPa)
CFM	28.04	11.83	11.83	6.10[a]	0.33	0.30[a]	0.30[a]	4.45[a]	0.62	0.62
MD	44.90	18.23	18.23	8.96[a]	0.32	0.32[a]	0.32[a]	5.36[a]	1.97[a]	1.97[a]

[a] Theoretical values calculated from equations in [21].

Table 1 Engineering elastic constants of laminates.

Specimen	Thickness	Crack initiation		Ultimate state[a]		Final delamination	
		Deflection	Load	Deflection	Load	Area	Symmetry ratio
	(mm)	(mm)	(kN)	(mm)	(kN)	(mm^2)	(-)
CP40-1	16.92	3.4	23.1	16.7	92.2	38015	0.64
CP40-2	16.77	3.0	20.0	16.8	91.9	34245	0.70
CP40-3	14.99	2.9	16.9	16.2	90.5	35195	0.95
CP40-4	16.57	3.0	20.5	17.6	93.2	46810	0.81
CP40-5	16.01	2.7	19.2	15.4	87.9	34609	0.91
CP80-1	15.79	3.1	15.1	16.4	93.4	35735	0.89
CP80-2	17.24	3.1	19.1	15.3	95.8	32123	0.92
CP80-3	17.21	3.5	19.8	14.8	90.1	38362	0.84

[a] The state when ultimate load was reached.

Table 2 Specimen list and experimental result summary.

2.2 Experimental set-up

The 2D experiments were conducted at laboratory conditions using a Zwick 500-kN universal testing machine. As shown in Fig. 2, The circular specimens were “semi-clamped” between two steel ring-shaped frames using eight screws. The upper frame had an inner radius of 150 mm, while the lower frame had an inner radius of 145 mm with a 5-mm-radius fillet, forming a support radius of 150 mm. The term “semi-clamp” refers to the specific boundary condition, where the out-of-plane degrees of freedom were constrained by the frames whole releasing the in-plane movement. This was achieved by inserting Teflon films with graphite lubricant between the contact surfaces of the specimens and frames to create nearly frictionless contact. In order to avoid stress concentration at the loading point, the bottom of the loading block was machined into a spherical surface with a radius of 300 mm, and a 3-mm thick rubber pad was placed between the loading block and the specimens.

The specimens were loaded under displacement-control at a rate of 1 mm/min. The load and displacement were recorded by the machine at a frequency of 2 Hz. A Linear Variable Differential Transducer (LVDT) measured the central deflection (hereafter referred to as “deflection” unless otherwise specified). The delamination growth was recorded by a digital video camera positioned above the specimens. Three rulers were stamped on the plate surface for measuring crack lengths in the north (N), west (W) and south (S) directions by visually analyzing the video frames (see Fig. 3). In addition, a 3D Digital Image Correlation System (DIC) was used to obtain deformation measurements of the top surface of the east sector, and an optical fiber was bonded to the top surface to measure the radial strains in the N and S directions. A video camera placed below the specimens recorded potential flexural damage propagation at the bottom center.

Prior to the main loading process, an in-situ debonding procedure was performed to create a proper pre-crack. The specimens were loaded under displacement-control for a small displacement until a sharp drop in load occurred, indicating the separation of the Teflon film. After unloading, the main loading process began immediately. In general, the 2D experiments resembled an ELS configuration in the radial direction (although with additional rotational constraints at the loading point due to the structural continuity and symmetry.

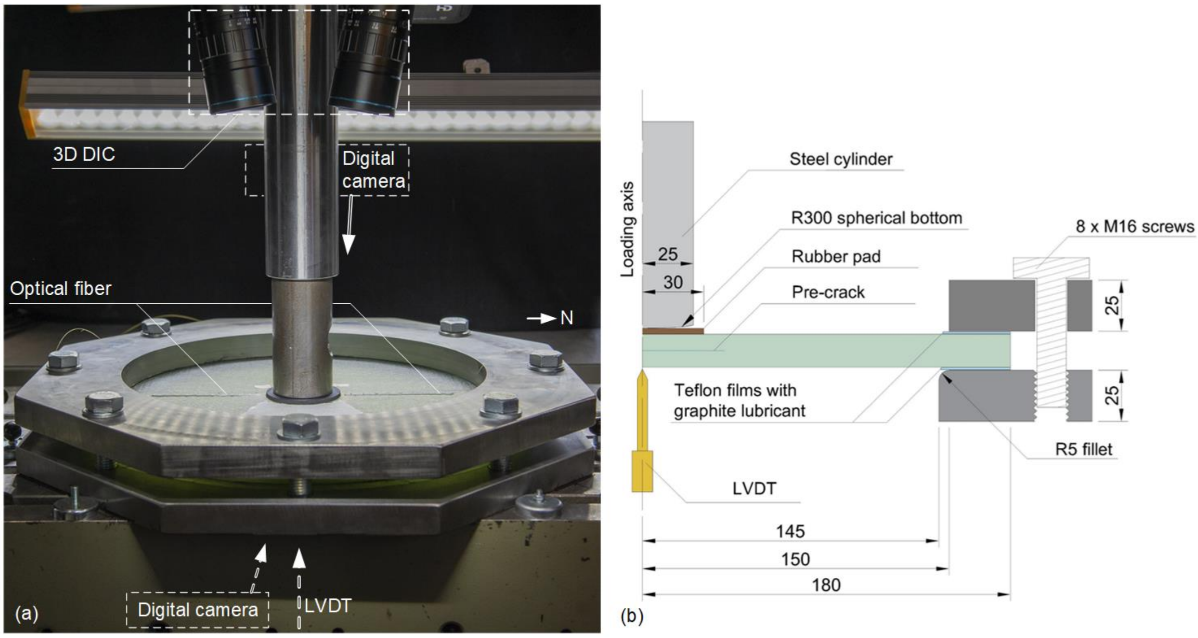

Fig. 2. Experimental set-up for 2D delamination: (a) photograph; (b) schematic profile (unit: mm).

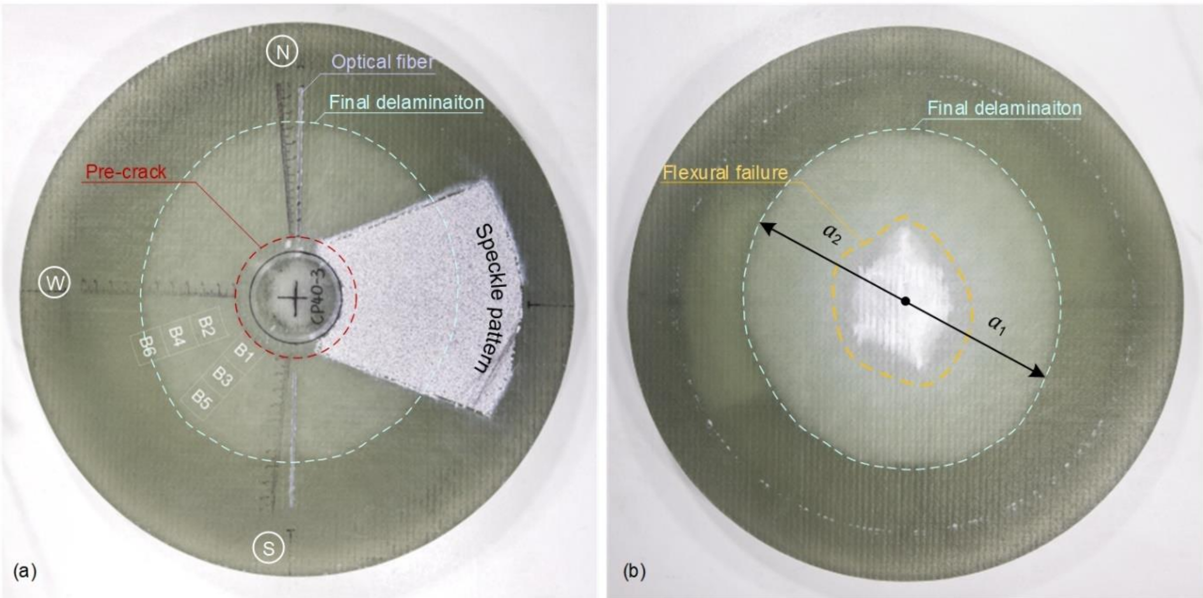

Fig. 3. Specimen CP40-3 after loading.

3 EXPERIMENTAL RESULTS

3.1 Failure mode and delamination pattern

All 2D specimens exhibited flexural failure at the center of the bottom surface after substantial delamination growth due to increasing tensile stresses (see Fig. 3). As the flexural failure extended, a secondary failure mechanism occurred, leading to a sharp drop in load. Failure inspection of the cut section of the specimens showed flexural failure in the lower sub-laminate and shear failure in the upper sub-laminate.

The main delamination grew in the mid-plane, except in some cases where the crack kinked into adjacent layer interfaces in the last centimeter of propagation after flexural failure. Despite certain asymmetry shown in the final delamination due to factors like eccentric loading, rubber pad instability, friction variation, and material inhomogeneity, all specimens reached a similar delamination area except for specimen CP40-4. The extent of asymmetry was quantified by the symmetry ratio of the final delamination, defined as the lowest value of the crack-length ratio between a diametric pair in all directions, e.g., a_1/a_2 for specimen CP40-3 in Fig. 3b. The results are listed in Table 2.

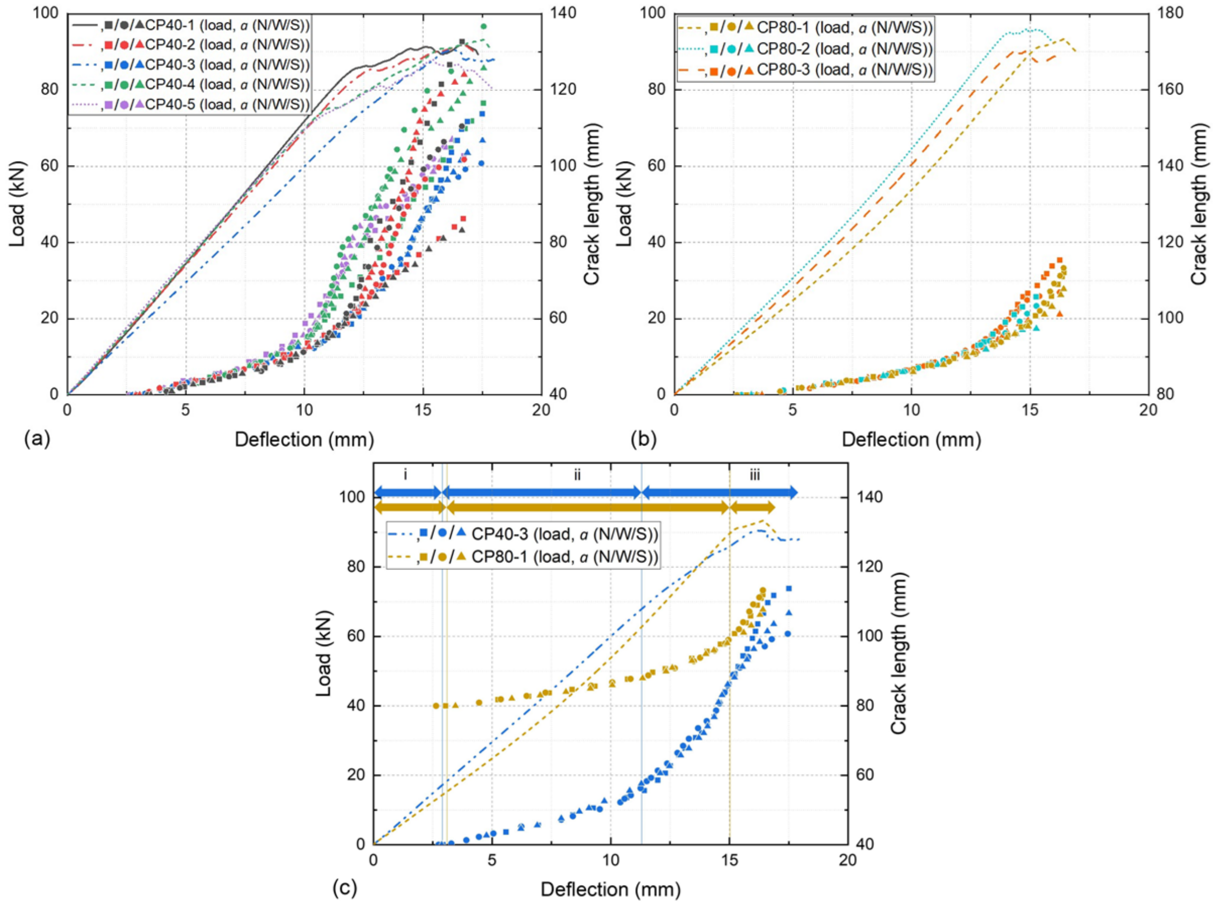

Fig. 4. Load and crack length vs deflection curves for (a) specimens with pre-crack radius of 40 mm, (b) specimens with pre-crack radius of 80 mm and (c) specimens CP40-3 and CP80-1.

3.2 Load, deflection and crack length

Table 2 summarizes the experimental results for each specimen. It includes the deflection and load at crack initiation (hereafter referred to as "initiation deflection" and "initiation load"), as well as the ultimate load and the corresponding deflection (hereafter referred to as the “ultimate deflection”, with the state defined as the "ultimate state"). Fig. 4 presents the load-deflection curves for both specimen groups. In the group with smaller pre-cracks (Fig. 4a), the curves show a linear increase in load up to 10-12 mm deflection despite crack initiation and propagation, followed by a reduced slope. In the group with larger pre-cracks (Fig. 4b), the load increased nonlinearly up to ~90 kN, indicating a stiffening phenomenon even with crack propagation. Subsequently, the specimens also underwent a stiffness drop, followed by failure. Crack-length measurements in the N/W/S directions are plotted alongside the load-deflection curves. The crack propagation exhibited a two-segment trend in the first group, with slower propagation in the beginning followed by a rapid increase in the propagation rate. Good symmetry was observed initially, but asymmetry arose during rapid propagation or near the ultimate state. Although the crack-length plots of the second segment lie in a wide band, similar slopes (i.e., propagation rates) can be noted. In the second group, only the first segment is identifiable due to limited delamination growth.

For comparison, the load and crack-length results of specimens CP40-3 and CP80-1 are displayed together in Fig. 4c. Despite different loading histories and energy dissipation, both specimens achieved comparable ultimate loads and deflections. The crack length vs deflection curves tended to converge at the end, indicating similar delamination sizes and growth rates. Based on the delamination behavior, three stages are defined: (i) crack initiation, (ii) slow propagation, and (iii) rapid propagation. The extent of deflection achieved in these stages varied with the pre-crack sizes. Specimen CP40-3 exhibited faster crack propagation and enters stage (iii) at a smaller deflection, while CP80-1 stayed longer in stage (ii), since the larger pre-crack radius of CP80-1 required more energy for early crack propagation compared to CP40-3.

3.3 Compliance behavior

Specimens CP40-3 and CP80-1 were selected to analyze the changes in structural compliance as a function of delamination area (derived from the average crack length in the three ruler directions by assuming a circular delamination shape throughout the loading process), as shown in Fig. 5. The compliance, calculated as the deflection (δ) over the load (P), exhibited a low point followed by a continuous rise for both specimens. The steep ascending segment after a 30,000-mm² crack area for CP40-3 indicated asymmetric delamination growth near the ultimate state. The low points marked the transition from stage (ii) to (iii) identified previously. In stage (ii), similar crack propagation lengths were achieved for both specimens, but due to the pre-crack radii, it constituted a smaller proportion of the crack-area increase in CP40-3 compared to CP80-1. The compliance variation resulted from the competition between stiffening mechanism, i.e., stretching, and the softening mechanism, i.e., delamination growth. Stretching occurred during bending, since the inward movement of the outer part of the plate was limited by the associated circumferential compression effect, making the outer part act like a frame, which constrained the in-plane deformation of the inner part and introduced radial tensile stresses. the stiffening effect from stretching intensified with increasing deflections. Delamination growth contributed to softening, while effect was weakened by the associated resistant mechanisms such as resin plastic deformation, microcracking (oriented 45° from the main delamination path near the tip, creating more fracture surfaces) and fiber bridging.

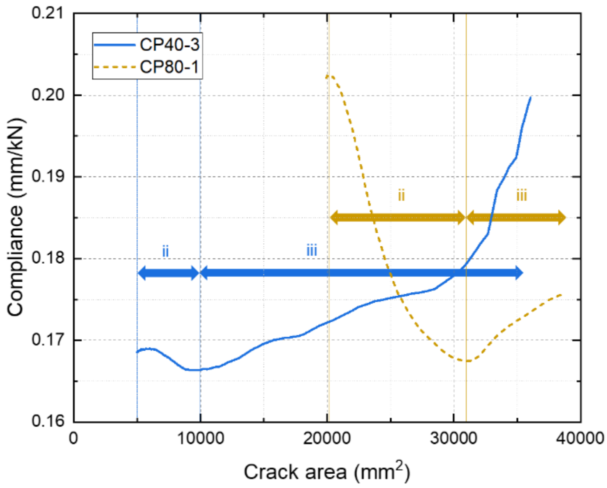

Fig. 5. Compliance vs crack area curves for specimens CP40-3 and CP80-1.

3.4 Delamination inspection

To directly observe the FPZ in the 2D experiments, six small rectangular samples were waterjet cut from the delaminated region of specimen CP40-3, as shown in Fig. 3a. Surprisingly, none of the samples split completely. Even sample B1, located approximately 5 cm behind the final delamination front, was still bridged by individual fibers, suggesting a FPZ length of at least 5 cm. The lateral surfaces of the samples were examined using a digital microscope. Samples B1 to B3 were opened in a controlled manner to investigate the fiber bridging condition, while samples B4 to B6 were kept in their original condition. The delamination condition of each sample was inspected and analyzed, as shown in Fig. 6. The examination revealed that as the surfaces approached the crack tip, they were gradually bridged by individual fibers, partially broken fiber bundles, and less damaged fiber bundles. The rough crack surfaces and the existence of fiber bundles lying on the delamination plane in various directions revealed significant ply nesting, which acted as a crack-arrest mechanism, increasing the fracture resistance. Hackles oriented ~45° from the main delamination plane were identified closer to the crack tip, indicating the formation of microcracks during the fracture process. The microcracking zone, spanning several hundred μm as shown in Fig. 6f, was considered to be located behind the crack tip in this work, since the material properties within the region were significantly reduced.

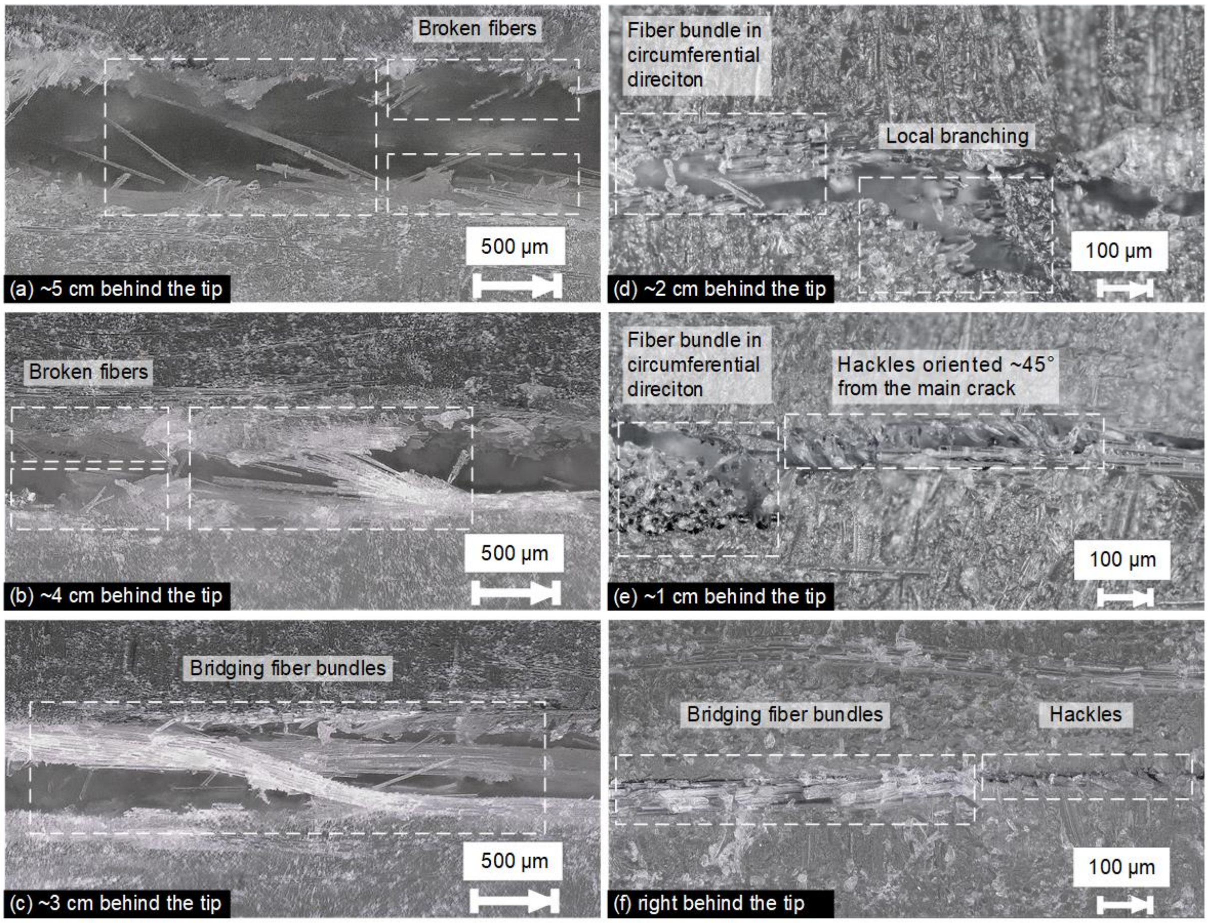

Fig. 6. Delamination in specimen CP40-3: samples (a) B1, (b) B2 and (c) B3 with ~1-mm opening; samples (d) B4, (e) B5 and (f) B6 in original conditions (arrows on scales pointing at crack front).

3.5 Validation of boundary conditions

Fig. 7 shows the variation of the radial displacement against deflection for a point located 132.4 mm from the center on the top surface (the farthermost point available for analyses) of specimen CP40-3, extracted from DIC data. This point is close to the boundary (r=150 mm), and hence the radial displacement can be used for an estimation of the relative slippage between the plate and clamping frames. As shown in the figure, the curve is smooth during the whole loading process, and most importantly, the slippage occurred immediately as the plate deflected without a lag, suggesting a frictionless movement. Thus, the validity of the semi-clamping boundary condition assumed in the experimental set-up can be confirmed.

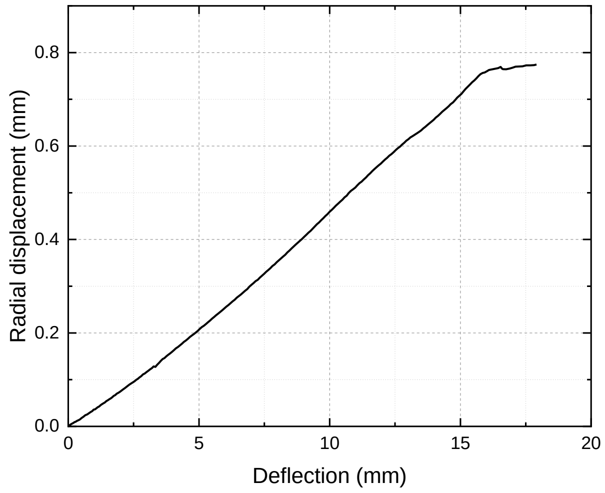

Fig. 7 Radial displacement at r=132.4 mm on top surface of specimen CP40-3

4 DISCUSSION

4.1 Fracture process zone

The conventional classification of the FPZ into a tip zone and a fiber bridging zone is not suitable for this study, since the formation and full development of fiber bridging did not significantly affect the load-deflection response or crack propagation rate. Instead, a new criterion based on traction between the delamination surfaces was used to divide the FPZ into a strong traction zone (STZ) near the crack tip and a weak traction zone (WTZ) at the wake. The STZ corresponded to the delamination states within a certain distance behind the crack tip, i.e., samples B4, B5 and B6 (Fig. 6d, e and f), where resin plastic deformation, microcracking, and strong fiber-bundle bridging occurred, preventing macro-separation of the delamination interface. The full development of the STZ marked the transition from slow to rapid crack propagation, similar to the role of full development of fiber bridging in 2D Mode-I delamination as reported in Ref. [22, 24]. The radial length of the fully developed STZ corresponded to the crack propagation length in the slow propagation stage. The WTZ, consisting of partially broken fiber bundles and individual fibers, was not fully developed until the end of the 2D experiments. The appearance of the WTZ led to separation of the crack surfaces, resulting in reduced structural stiffness and increased crack propagation rate. The crack-length plots indicated a constant propagation rate after full development of the entire FPZ in 2D delamination.

4.2 Effect of pre-crack size

Fig. 8 presents the effects of the pre-crack size on the crack initiation and ultimate states of the experiments. Doubling the pre-crack radius led to the crack initiating at a 7% larger deflection and 11% lower load due to the increase in the crack-front length and the decrease in initial stiffness. The ultimate state showed a 6% smaller deflection and 2% higher load for larger pre-cracks, and the final delamination area decreased by 6%. To explain the results, two ideal specimen cases with the same parameters (material properties, thickness, etc.), except that a_0=40 mm for Case 1 and a_0=80 mm for Case 2, are employed. Even when Case 1 is pre-cracked by loading it until a=80 mm and then unloading, it is still different from Case 2 due to the presence of the large-scale FPZ. The extra traction forces from the FPZ in the region between 40 mm<r<80 mm (radial coordinate) slightly strengthen Case 1 during subsequent loading, compared to Case 2. As a result, Case 1 requires a larger crack size at failure to compensate the strengthening effect which redistributes stresses in a more favorable state. On the other hand, Fig. 4c shows that Case 1 needs larger deflection and load to reach the same crack length as Case

2 (a>80 mm) to close the gap in a_0, meaning even larger deflection and load to achieve a larger crack size at failure, as mentioned above. Overall, specimens with a smaller pre-crack exhibit larger deflection, load, and delamination area at the ultimate state. The experimental results in Fig. 8b agree with this analysis, except for the ultimate load due to experimental scatter. After full development of the FPZ, the differences in load-deflection response and delamination growth resulting from different pre-crack sizes vanish, as shown in the converging trends of the load-deflection curves and crack-length plots in Fig. 4c.

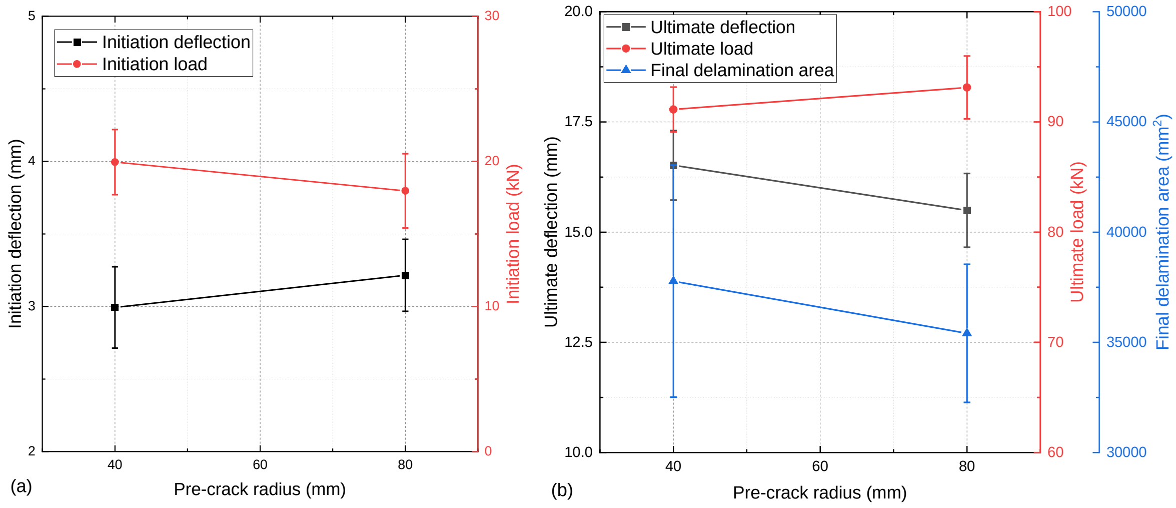

Fig. 8. Effects of pre-crack radius on (a) initiation load and deflection, and (b) ultimate load and deflection and final delamination area.

5 CONCLUSIONS

In this study, the 2D delamination growth in composite laminates under Mode-II fracture conditions was investigated using a novel experimental setup. The main findings and conclusions are as follows:

- The load initially increased with constant or increasing stiffness, depending on the pre-crack size, despite certain amount of delamination growth, and then continued to increase with reduced stiffness.
- The crack propagation exhibited a two-segment behavior. Initially, the crack propagated slowly with respect to the increase in deflection (first segment), and then the propagation rate accelerated noticeably (second segment). Accordingly, the loading process was divided into three stages: crack initiation, slow propagation (first segment), and rapid propagation (second segment). For specimens with a smaller pre-crack, the slow and rapid crack propagation stages contributed equally during the whole loading process, and most of the delamination area was generated during the rapid propagation stage. However, for 2D specimens with a larger pre-crack, the slow crack propagation stage dominated the loading process, and similar amounts of delamination area were created in both slow and rapid crack propagation stages.
- The fracture process zone exhibited matrix plastic deformation, hackles indicating microcracking, and fiber/bundle bridging. It could be divided into a strong traction zone near the crack tip, where the crack surfaces were firmly connected by deformed resin and intact fiber bundles, and a weak traction zone, where the crack surfaces were separated but bridged by partially broken fiber bundles and individual fibers. The full development of the strong traction zone was responsible for the transition from slow to rapid crack propagation.
- Under quasi-static Mode-II loading, crack propagation did not result in catastrophic failure, as the load continued to increase with further deflection, indicating a pseudo-ductility effect. If the fracture process zone could fully develop before failure, the ultimate load, deflection,

and delamination area would be independent of the pre-crack size. However, in practice, a larger pre-crack would generally lead to a more significant reduction in structural performance, as delaminated structures often fail before achieving full development of the fracture process zone.

ACKNOWLEDGEMENTS

The authors wish to acknowledge the financial support of this research by the Swiss National Science Foundation (Grant No. 200020_185005) and the assistance provided by the technical team of the structural engineering experimental platform (GIS-ENAC at the Ecole Polytechnique Fédérale de Lausanne (EPFL), Switzerland. The authors wish also to thank Owens Corning, United States, for the supply of the CFM reinforcements.

REFERENCES

[1] S. Sridharan, *Delamination Behaviour of Composites*. Cambridge, England: Woodhead Publishing Limited, 2008. (doi: 10.1533/9781845694821).

[2] ISO 15024:2001, *Fibre-Reinforced Plastic Composites — Determination of Mode I interlaminar Fracture Toughness, Gic, for Unidirectionally Reinforced Materials*. 2001.

[3] ISO 15114:2014, *Fibre-reinforced plastic composites — Determination of the mode II fracture resistance for unidirectionally reinforced materials using the calibrated end-loaded split (C-ELS) test and an effective crack length approach.* 2014.

[4] ASTM D7905/D7905M-19e1, Standard test method for determination of the mode II interlaminar fracture toughness of unidirectional fiber-reinforced polymer matrix composites. 2019. (doi: 10.1520/D7905_D7905M-19E01).

[5] A. D6671M, Standard Test Method for Mixed Mode I-Mode II Interlaminar Fracture Toughness of Unidirectional Fiber Reinforced Polymer Matrix Composites, 2006, p. 15 (doi: 10.1520/D6671).

[6] M. Shahverdi, A. P. Vassilopoulos, and T. Keller, Mixed-mode quasi-static failure criteria for adhesively-bonded pultruded GFRP joints, *Composites Part A: Applied Science and Manufacturing*, **59**, 2014, pp. 45–56 (doi: 10.1016/j.compositesa.2013.12.007).

[7] B. R. K. Blackman, A. J. Brunner, and J. G. Williams, Mode II fracture testing of composites: a new look at an old problem, *Engineering Fracture Mechanics*, **73** (16), 2006, pp. 2443–2455 (doi: 10.1016/j.engfracmech.2006.05.022).

[8] L. Sorensen, J. Botsis, T. Gmür, and L. Humbert, Bridging tractions in mode I delamination: Measurements and simulations, *Composites Science and Technology*, **68** (12), 2008, pp. 2350–2358 (doi: 10.1016/j.compscitech.2007.08.024).

[9] W. Gong, J. Chen, and E. A. Patterson, An experimental study of the behaviour of delaminations in composite panels subjected to bending, *Composite Structures*, **123**, 2015, pp. 9–18 (doi: 10.1016/j.compstruct.2014.12.008).

[10] K. F. Nilsson, J. C. Thesken, P. Sindelar, A. E. Giannakopoulos, and B. Stoåkers, A theoretical and experimental investigation of buckling induced delamination growth, *Journal of the Mechanics and Physics of Solids*, **41** (4), 1993, pp. 749–782 (doi: 10.1016/0022-5096(93)90025-B).

[11] A. T. Rhead, R. Butler, and G. W. Hunt, Compressive strength of composite laminates with delamination-induced interaction of panel and sublaminate buckling modes, *Composite Structures*, **171**, 2017, pp. 326–334 (doi: 10.1016/j.compstruct.2017.03.011).

[12] L. B. Andraju, M. Ramji, and G. Raju, Snap-buckling and failure studies on CFRP laminate with an embedded circular delamination under flexural loading, *Composites Part B: Engineering*, **214**, 2021, p. 108739 (doi: 10.1016/j.compositesb.2021.108739).

[13] A. Riccio, A. Raimondo, F. Di Caprio, and F. Scaramuzzino, Delaminations buckling and growth phenomena in stiffened composite panels under compression. Part II: A numerical study, *Journal*

of Composite Materials, **48** (23), 2014, pp. 2857–2870 (doi: 10.1177/0021998313502742).

[14] G. A. O. Davies, X. Zhang, G. Zhou, and S. Watson, Numerical modelling of impact damage, *Composites*, **25** (5), 1994, pp. 342–350 (doi: 10.1016/S0010-4361(94)80004-9).

[15] G. A. O. Davies and X. Zhang, Impact damage prediction in carbon composite structures, *International Journal of Impact Engineering*, **16** (1), 1995, pp. 149–170 (doi: 10.1016/0734-743X(94)00039-Y).

[16] D. D. R. Cartié and P. E. Irving, Effect of resin and fibre properties on impact and compression after impact performance of CFRP, *Composites Part A: Applied Science and Manufacturing*, **33** (4), 2002, pp. 483–493 (doi: 10.1016/S1359-835X(01)00141-5).

[17] A. Tabiei and W. Zhang, Composite laminate delamination simulation and experiment: A review of recent development, *Applied Mechanics Reviews*, **70** (3), 2018, pp. 1–23 (doi: 10.1115/1.4040448).

[18] S. N. Chatterjee, W. A. Dick, and R. Byron Pipes, Mixed-mode delamination fracture in laminated composites, *Composites Science and Technology*, **25** (1), 1986, pp. 49–67 (doi: 10.1016/0266-3538(86)90020-5).

[19] G. A. O. Davies, P. Robinson, J. Robson, and D. Eady, Shear driven delamination propagation in two dimensions, *Composites Part A: Applied Science and Manufacturing*, **28** (8), 1997, pp. 757–765 (doi: 10.1016/S1359-835X(97)00015-8).

[20] P. Kumar and S. R. Reddy, Experimental determination of interlaminar GIc using a fully embedded centre-cracked specimen, *Engineering Fracture Mechanics*, **59** (2), 1998, pp. 183–189 (doi: 10.1016/S0013-7944(97)00096-9).

[21] A. Cameselle-Molares, A. P. Vassilopoulos, and T. Keller, Experimental investigation of two-dimensional delamination in GFRP laminates, *Engineering Fracture Mechanics*, **203**, 2018, pp. 152–171 (doi: 10.1016/j.engfracmech.2018.05.015).

[22] A. Cameselle-Molares, A. P. Vassilopoulos, J. Renart, A. Turon, and T. Keller, Numerical simulation of two-dimensional in-plane crack propagation in FRP laminates, *Composite Structures*, **200**, 2018, pp. 396–407 (doi: 10.1016/j.compstruct.2018.05.136).

[23] A. Cameselle-Molares, A. P. Vassilopoulos, J. Renart, A. Turon, and T. Keller, Numerically-based method for fracture characterization of Mode I-dominated two-dimensional delamination in FRP laminates, *Composite Structures*, **214**, 2019, pp. 143–152 (doi: 10.1016/j.compstruct.2019.02.014).

[24] C. Wang, A. P. Vassilopoulos, and T. Keller, Numerical modeling of two-dimensional delamination growth in composite laminates with in-plane isotropy, *Engineering Fracture Mechanics*, **250**, 2021, p. 107787 (doi: 10.1016/j.engfracmech.2021.107787).

[25] J. Wen, Z. Xia, and F. Choy, Damage detection of carbon fiber reinforced polymer composites via electrical resistance measurement, *Composites Part B: Engineering*, **42** (1), 2011, pp. 77–86 (doi: 10.1016/j.compositesb.2010.08.005).

[26] ISO 527-4:2021(E), *Plastics — Determination of tensile properties — Part 4:Test conditions for isotropic and orthotropic fibre-reinforced plastic composites*. 2021.

[27] ISO 19927:2018, *Fibre-reinforced plastic composites — Determination of interlaminar strength and modulus by double beam shear test*. Geneva, Switzerland, 2018.